Structures 56 (2023) 105006

Contents lists available at ScienceDirect

Structures

journal homepage: www.elsevier.com/locate/structures

A mixed micromechanical homogenisation scheme for the prediction of the 3D orthotropic elastic properties of different masonry bond typologies

Anastasios Drougkas *

Serra Húnter Fellow, Department of Strength of Materials and Structural Engineering, Universitat Politècnica de Catalunya (UPC-BarcelonaTech), C/Colom 11, 08222 Terrassa, Spain

ARTICLE INFO

Keywords:
Homogenisation
Micromechanics
Orthotropic elasticity
Masonry

ABSTRACT

Masonry structures composed of two distinct material phases (units and mortar) with potentially vastly different elastic properties are characterised by strong orthotropy. The variety of commonly employed bond typologies for masonry walls, featuring unit groups and mortar joints with different orientation with respect to the plane of the wall, result in complex stress and strain interactions between the material phases. This interaction is further complicated by the high volume ratio of the units within the masonry composite. Therefore, classical homogenisation schemes for matrix-inclusion composite materials, mortar being the matrix and units the inclusions, are suitable for only a narrow range of relative unit and mortar stiffness, expressed as the ratio of the Young's moduli of the two phases. This feature makes their application in nonlinear analysis of masonry structures, which have a strong tendency to crack under mechanical loading, problematic.

The paper presents a novel homogenisation scheme based on different mean-field homogenisation schemes combined through a process derived from the discretisation of the masonry cells using a method-of-cells approach. This approach allows the intuitive interpretation of the stress and strain interaction of the material phases and yields good predictions of the elastic properties of a variety of masonry bonds over an extensive range of relative unit and mortar stiffness.

1. Introduction

Masonry construction is a widespread structural typology, encompassing a wide array of different bonding patterns and accounting for a large percentage of the inventory of existing structures, such as vernacular and monumental buildings and infrastructure. Therefore, the accurate prediction of the behaviour of masonry structures under mechanical loading caused by tectonic [21] or induced [16] earthquake action or differential settlement [14] has important financial, social and cultural implications.

The structural analysis of masonry structures is complicated due to their construction using materials, namely the units and the mortar, with potentially very different mechanical properties, bonded in widely different bonding patterns, in single- or double-wythe layouts. Even when considering isotropic properties for the material phases, orthotropy arises in the masonry as a whole due to these bonding patterns [26,25,29]. A further implication of the different properties of the material phases of masonry is their widely different mechanical strength and durability. Consequently, the detection of damage in masonry structures using structural monitoring techniques ideally needs to be performed at the material level of the units and mortar [17]. Thus, the structural analysis component of digital twinning operations on masonry structures needs to be able to provide stress–strain data at the material level instead of at the level of the composite.

The orthotropy of masonry can be modelled through approaches that take into account the stress–strain interaction of the material phases. Direct finite element simulation of the material phases of masonry provides data on the stress–strain condition of each material phase with the highest level of geometrical fidelity [9,10,23,34]. However, these approaches are prohibitively cumbersome for the analysis of large structures and for the efficient processing and interpretation of the generated data.

As an alternative to such computationally-intensive approaches, analytical models developed for the analysis of composite materials composed of a matrix with embedded inclusions comprise a useful and flexible family of tools in efforts to accurately simulate masonry structures. Such schemes can be adopted for the simulation of either regularly-bonded masonry [2,7,33,36] or be suitably adapted to

* Corresponding author.
E-mail address: anastasios.drougkas@upc.edu.

https://doi.org/10.1016/j.istruc.2023.105006
Received 21 March 2023; Received in revised form 21 June 2023; Accepted 31 July 2023
Available online 8 August 2023

consider irregularly-bonded masonry through statistical approaches [5–6].

In adopting micromechanical models for the analysis of masonry, the mortar can usually be treated as the matrix and the units as the embedded inclusions [4,11,12], although inverse and mixed approaches have also been developed [38] in order to more directly capture the finer geometrical details of the units and mortar within the composite. Method-of-cells approaches [1] suitably adapted for the linear [39] and nonlinear analysis [8] of masonry composites have also been developed in an effort to more naturally capture the geometrical arrangement of the matrix and inclusions in the composite. These approaches too, however, despite their accuracy, are cumbersome to apply in double-wythe masonry typologies due to the difficulty in deriving the large number of analytical stress–strain relations between the individual cells. Regardless of the underlying assumptions and general approach, implementation of these homogenisation schemes allows capturing the complex mechanical behaviour of masonry structures through finite element macromodels, thus eliminating the requirements for full geometrical representation of the masonry bond and facilitating the detailed analysis of large structural systems. Further, these methods are typically only applicable in the case of units embedded in mortar, namely with all joints (bed, head and transversal) completely filled. Further, very thin joints may render these approaches inaccurate due to the resulting low volume ratio of the mortar matrix. In such cases, empirical homogenisation techniques may be more suitable [19].

Simple mean-field homogenisation methods can be employed as a first step in the determination of the elastic properties of composite materials. These include classical approaches, such as the Reuss [31] and Voigt [35] schemes, usually accepted as providing a lower and upper bound for the stiffness of the composite. These schemes can be enhanced by taking into account the Poisson's ratios of the material phases for obtaining a more realistic interaction between them [24]. This is an important refinement of the classical schemes given the strong influence of the Poisson's ratios of the phases on the elastic properties and nonlinear response of the composite [13]. Even so, and despite the simplicity of their implementation, these schemes fail to take into account finer geometric details for the matrix and inclusions which are the main source of the differences between the properties of different masonry bond typologies. Additionally, these schemes tend to lose accuracy for diverging relative stiffness of the phases, namely they are accurate for phases of roughly equal stiffness. This fact makes their application in nonlinear analysis, where typically one of the phases will have an effective stiffness tending to 0, problematic.

Additional geometric information related to the inclusions as well as their interaction in tightly-packed configurations in a composite can be introduced through the adoption of the Mori-Tanaka scheme [27]. This mean-field homogenisation scheme introduces more geometrical information regarding the inclusions, most importantly the aspect ratio and orientation with respect to the axes of the composite material. Nevertheless, geometrical information related to the matrix is not taken into account. This is in stark contrast with the actual stress–strain conditions encountered in masonry under different states of macroscopic applied stress. For instance, in the common case of running bond masonry the bed joints are in nearly isostress conditions when the composite is subjected to vertical or in-plane shear stresses, while the head joints are only partially in isostress conditions when the composite is subjected to horizontal stresses.

The principal objective of the present paper is the development of a mixed mean-field homogenisation scheme for the most common bond types for masonry walls: stack, running, English and Flemish bond. The scheme was designed to take into account using a unified approach the different stress–strain conditions encountered in different parts of the mortar matrix in order to more accurately model the interaction of units and mortar in the composite. Further, the was designed to be able to consider different groups of units, namely units with both longitudinal and transversal orientation with respect to the plane of the wall. Finally, the proposed scheme was required to be characterised by low computational cost in order to be competitive with homogenisation methods based on finite element calculations. The proposed model was validated against a finite element benchmark over a wide range of material and geometric properties. Finally, the proposed model was compared against the Mori-Tanaka mean-field homogenisation scheme for demonstrating the increase in accuracy compared to more classical homogenisation approaches.

2. Derivation of masonry periodic unit cells

Overall, the derivation of the masonry periodic unit cell (PUC) for each of the bonding patterns examined relies on the identification of a repeating geometric pattern and its subdivision into macroscopically distinct sectors, or cuboids.

Four different types of PUC for masonry wall typologies were studied in this paper: stack bond (SB), running bond (RB), English bond (EB) and Flemish bond (FB) (Figure 1). These bonding patterns, characterised by different unit interlocking patterns, represent a large percentage of the inventory of existing masonry structures constructed using regularly-sized brick or, less commonly, stone units. While masonries comprised of irregularly-sized units can be numerically studied using statistical techniques [11], the present study is limited to regularly-bonded masonries.

The two steps for the derivation of the PUCs for each of the considered masonry bonding patterns are presented in Figure 2. In the first step, the repeating geometric pattern is identified. Subsequently, the repeating pattern is further simplified due to the existence of three planes of symmetry. Also indicated in Figure 2 is the axis convention adopted in the study: x corresponds to the horizontal direction along the length of the wall, y corresponds to the vertical direction along the height of the wall and z corresponds to the transversal direction normal to the plane of the wall. The increase in the complexity of the bonding pattern and the introduction of a combination of stretcher and header units in the EB and FB cases results in an increase in the size of the PUC.

The masonry PUCs were subdivided into cuboids corresponding to geometrically distinct entities within the cell in a manner similar to the one adopted in the method-of-cells approach for the analysis of composite materials [1]. The geometric interlocking of the units in each bonding pattern gives rise to distinct cuboids arranged in a three-dimensional orthogonal grid. Each cuboid belongs entirely to one material phase: mortar or unit. According to the derived grid, and based on the traditional naming convention of units and mortar joints in masonry, each cuboid corresponds to a specific type. Mortar cuboids can belong to

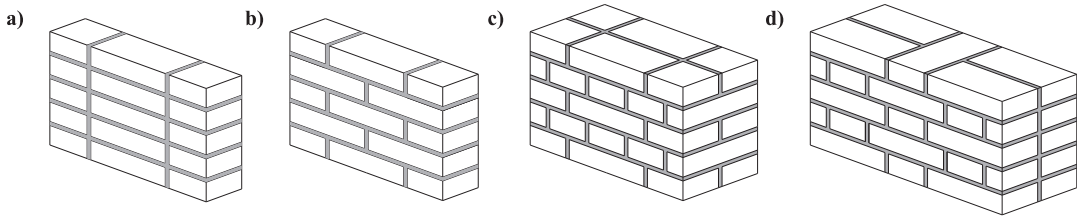

Fig. 1. Types of masonry bonding patterns investigated in the p resent paper: a) stack bond, b) running bond, c) English bond, d) Flemish bond.

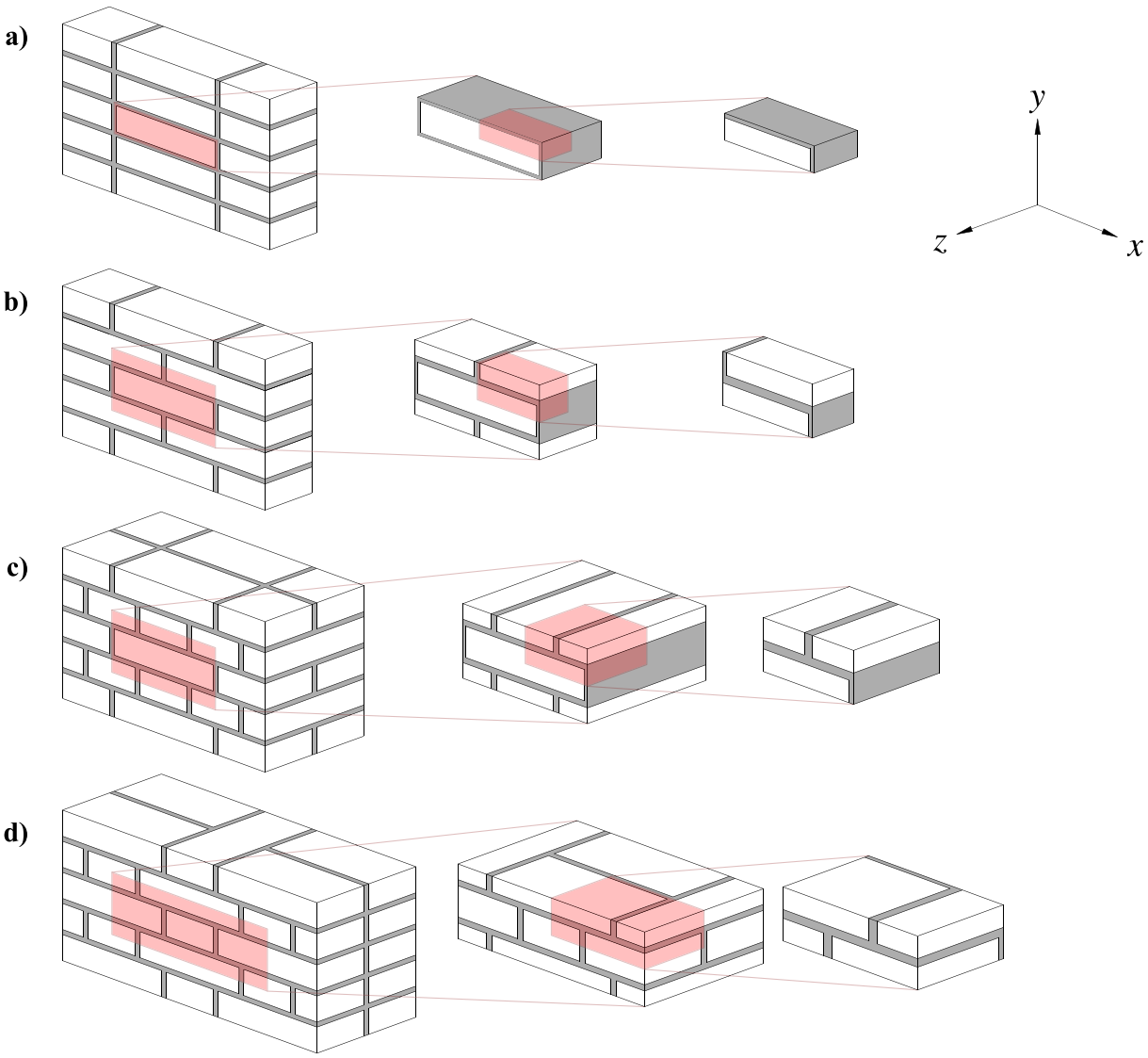

Fig. 2. Derivation of periodic unit cells for masonry bonding patterns. Identification of repeating geometric pattern and simplification due to symmetry: a) stack bond, b) running bond, c) English bond, d) Flemish bond.

bed (b), cross (c), head (h) or transversal (t) joints. Bed joints are oriented in the xz plane between the unit beds. Head joints are oriented in the yz plane adjacent to the units or between units. Transversal joints are oriented in the xy plane between units. Cross joints are defined as the remaining mortar cuboids, at the intersection between bed, head and transversal joints and represent a very low percentage of the total mortar volume. Unit cuboids can belong to either stretcher (s) or header (d) units. Stretcher units are oriented with their length along the x axis while header units are oriented with their length along the z axis. Each cuboid was further assigned a subindex for the purpose of identification. Cuboids with identical dimensions and function were assigned the same subindex for the purpose of simplicity.

The discretisation of the investigated bonding patterns into cuboids is shown in Figure 3. The naming convention for the dimensions of the components is also introduced here. Lengths along the x, y and z directions were designated with the parameters l, h and t respectively. Dimensions specific to the units and the mortar joints were designated with the subindices u and j respectively. As such, the length, height and width of the units were designated as l_u, h_u and t_u respectively, while the thicknesses of the head, bed and transversal joints are designated as l_j, h_j and t_j respectively. For maintaining geometric compatibility in the transversal direction in EB and FB walls, meaning that the header units do not protrude from the transversal face of the wall at the xy plane, it is required that:

$$l_u = 2t_u + t_j \tag{1}$$

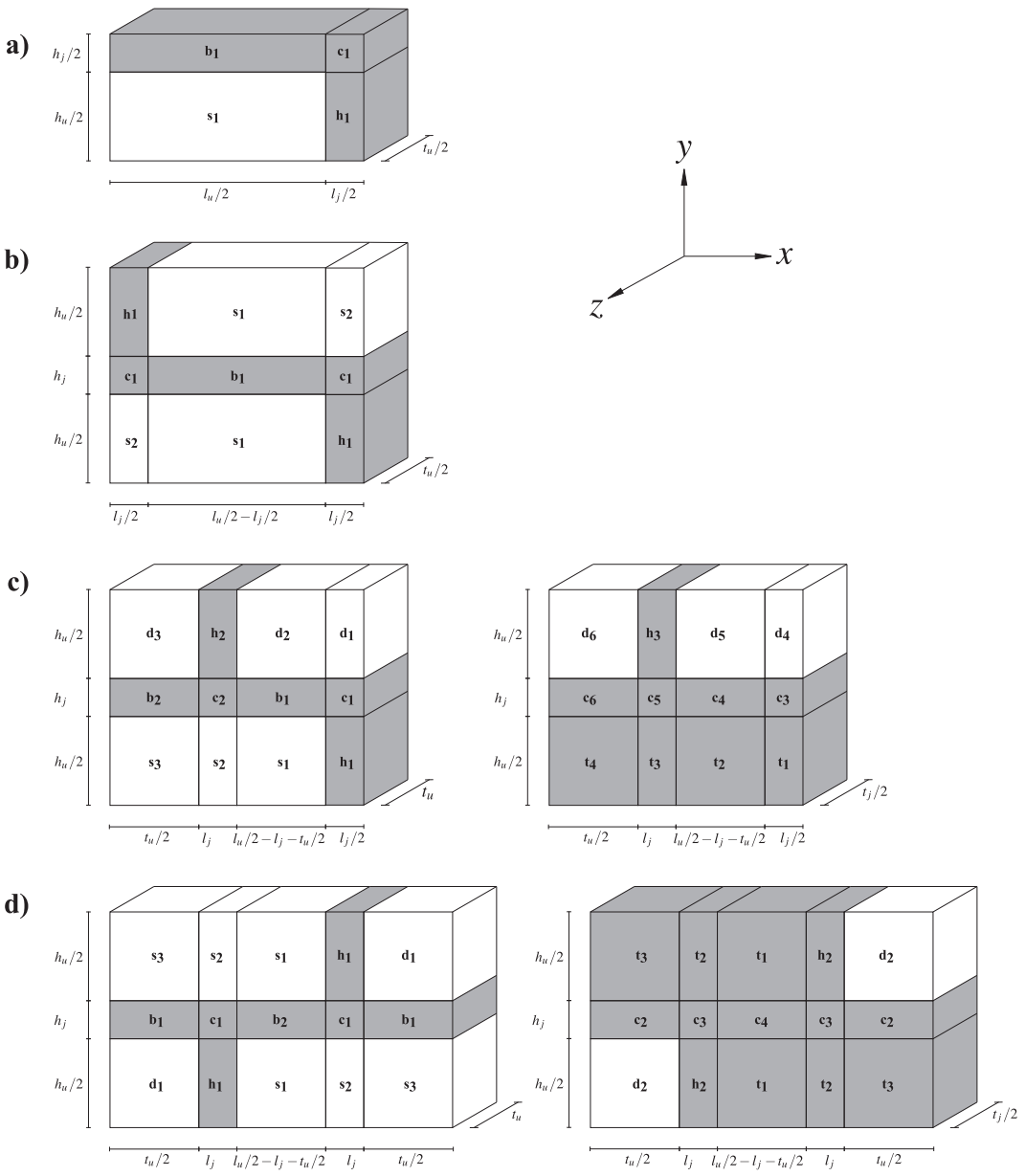

Fig. 3. Subdivision of masonry PUCs into cuboids: a) stack bond, b) running bond, c) English bond, d) Flemish bond.

The derived total orthogonal dimensions of the PUCs (length l_c, height h_c and width t_c) are presented in Table 1.

The total volume of each cell V_c is equal to the product of its three orthogonal dimensions:

$$V_c = l_c h_c t_c \tag{2}$$

Based on the dimensions of the cuboids, it is possible to determine the volume fractions for each of the unit and mortar types, namely the proportion of the volume taken up by each component with respect to the total volume of the PUC: ω_s for stretcher units, ω_d for header units, ω_b for bed joints, ω_c for cross joints, ω_h for head joints and ω_t for transversal joints. These volume fractions are equal to the volume fraction of the cuboid type with respect to the volume of the cell V_c. These volume fractions are expressed symbolically as a function of the characteristic dimensions of the units and joints in Table 2.

The total volume fractions of the phases (ω_u for the units and ω_j for the mortar joints) are calculated for each bonding pattern according to the expressions:

$$\omega_u = \omega_s + \omega_d$$

$$\omega_j = \omega_b + \omega_c + \omega_h + \omega_t = 1 - \omega_u \tag{3}$$

Finally, it is possible to calculate the relative volume fraction of each joint type designated as n with respect to the volume of the mortar phase as a whole using the expression:

$$\widehat{\omega}_n = \omega_n / \omega_j \tag{4}$$

Table 1
PUC dimensions for investigated bonding patterns.

Bond	l_c	h_c	t_c
SB	$l_u/2 + l_j/2$	$h_u/2 + h_j/2$	$t_u/2$
RB	$l_u/2 + l_j/2$	$h_u + h_j$	$t_u/2$
EB	$l_u/2 + l_j/2$	$h_u + h_j$	$t_u + t_j/2$
FB	$l_u/2 + t_u/2 + l_j$	$h_u + h_j$	$t_u + t_j/2$

Table 2
Volume fraction of each unit and mortar type for the investigated bonding patterns.

Bond	ω_s	ω_d	ω_b	ω_c	ω_h	ω_t
SB	$\frac{h_u l_u t_u}{8V_c}$	0	$\frac{h_j l_u t_u}{8V_c}$	$\frac{h_j l_j t_u}{8V_c}$	$\frac{h_u l_j t_u}{8V_c}$	0
RB	$\frac{h_u l_u t_u}{4V_c}$	0	$\frac{h_j t_u (l_u - l_j)}{4V_c}$	$\frac{h_j l_j t_u}{2V_c}$	$\frac{h_u l_j t_u}{4V_c}$	0
EB	$\frac{h_u l_u t_u}{4V_c}$	$\frac{(l_u - l_j) h_u (t_j + 2t_u)}{8V_c}$	$\frac{(l_u - 2l_j) h_j t_u}{2V_c}$	$\frac{h_j (l_j t_j + 6 l_j t_u + l_u t_j)}{4V_c}$	$\frac{l_j h_u (t_j + 3t_u)}{4V_c}$	$\frac{(l_j + l_u) h_u t_j}{8V_c}$
FB	$\frac{h_u l_u t_u}{2V_c}$	$\frac{(t_j + 2t_u) h_u t_u}{4V_c}$	$\frac{(l_u - 2l_j + t_u) h_j t_u}{2V_c}$	$\frac{h_j (2 l_j t_j + 8 l_j t_u + l_u t_j + t_j t_u)}{4V_c}$	$\frac{l_j h_u (t_j + 2t_u)}{2V_c}$	$\frac{l_u h_u t_j}{4V_c}$

$n = \{b, c, h, t\}$

3. Homogenisation scheme

3.1. Overview

The adopted analysis approach was that of a first-order two-scale model for masonry wall structures [18]. In this context, the wall structure comprises the macro-scale while the PUC comprises the micro-scale. The relation between strains and stresses in the coarse macro-scale is accomplished through an intermediate analysis step for the calculation of the finer stresses and strains in the micro-scale. A scheme of this process is presented in Figure 4. Firstly, for each sampling point in a structure, which would correspond to a Gauss point in a finite element analysis context, a macro-scale strain $\bar{\varepsilon}$ is defined and passed to the PUC. Secondly, the PUC is solved for this applied macro-strain under defined periodic boundary conditions, thus calculating the micro-scale stresses and strains. Finally, as a function of these micro-scale stresses and strains, the macro-scale stress $\bar{\sigma}$ at the sampling point is calculated.

Masonry was treated as a composite material with the mortar acting as the matrix and the units acting as the inclusions. All material phases were considered homogeneous and isotropic, although anisotropic inclusions can be readily considered without any modification of the method apart from the stiffness tensor of the inclusions. All analyses in the present study were performed under the conditions of linear elasticity, discounting possible changes in the stiffness of the constituent materials due to confinement or multi-axial loading. The homogenisation scheme developed here was a weighted combination of three classical mean-field homogenisation schemes: the Reuss [31], Voigt [35]and Mori-Tanaka [27] schemes. The classical Voigt and Reuss schemes ignore all geometric information regarding the inclusions and rely only on the volume fractions of the phases, while the Mori-Tanaka scheme additionally takes into account the shape of the inclusions. Therefore, the arrangement of the matrix within the composite, which can directly affect its stress and strain, is not included in any of these schemes. This is

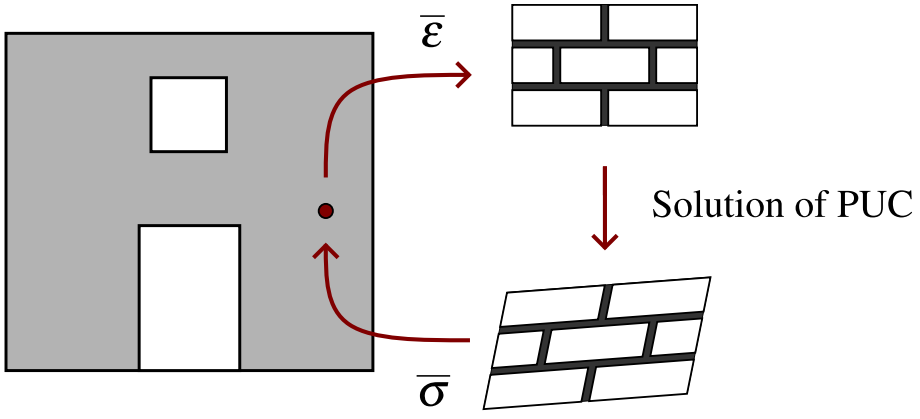

Fig. 4. First-order two-scale problem solution scheme.

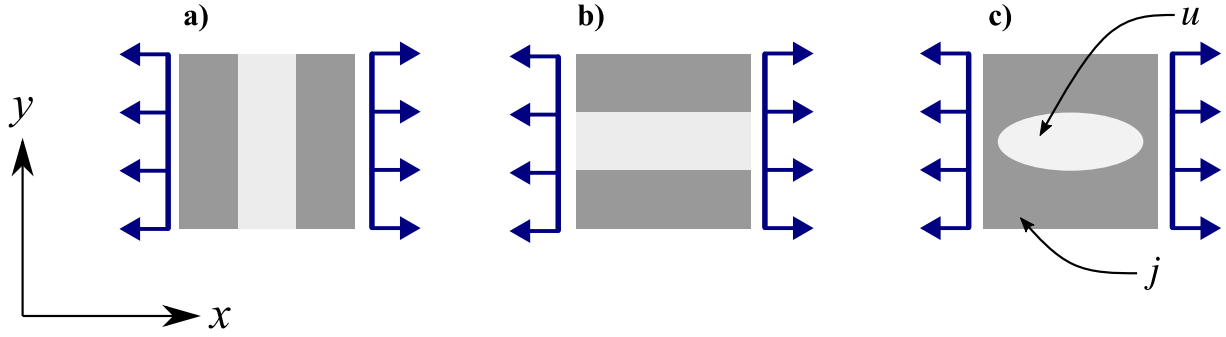

Fig. 5. Illustration of stress–strain conditions for macroscopic strain applied in the *xx* direction on a composite material consisting of a matrix *j* and embedded inclusions *u*: a) Reus, b) Voigt, c) dilute.

considered unrealistic given the patently different function of the bed, head and transversal joints to mechanical strains applied in different directions or planes. For example, the bed joints respond in a nearly isostress condition for loading in the *yy* direction or *xy* plane, while their confinement between the units in the *xx* direction means that they respond in a manner closer to isostrain conditions. This feature was addressed in the proposed scheme by applying weighing factors in a combination of the three schemes according to the relative volume fraction of the matrix participating in stress–strain conditions that can be described as isostrain, isostress or dilute for each loading component. Perfect bond between the material phases is considered in all three stress–strain conditions. The three stress–strain conditions in a two-phase composite material considered in this paper are schematically illustrated in Figure 5.

In contrast with other mixed mean-field schemes, founded on calibrated interpolations between individual schemes [22], iterative approaches [37] or on permutation between function of the matrix and inclusions[30], the scheme proposed here was based on an intuitive, closed-form, geometry-based weighted combination of classic schemes. Thus, neither the physical meaning of the interaction between phases nor the interpolation between constituent schemes is opaque.

3.2. Stiffness tensors for different stress–strain conditions

The three-dimensional stiffness tensor C_k of an isotropic material phase k with Young's modulus E_k and Poisson's ratio ν_k is equal to:

$$C_k = \frac{E_k}{(1+\nu_k)(1-2\nu_k)} \begin{bmatrix} 1-\nu_k & \nu_k & \nu_k & 0 & 0 & 0 \\ \nu_k & 1-\nu_k & \nu_k & 0 & 0 & 0 \\ \nu_k & \nu_k & 1-\nu_k & 0 & 0 & 0 \\ 0 & 0 & 0 & 1-2\nu_k & 0 & 0 \\ 0 & 0 & 0 & 0 & 1-2\nu_k & 0 \\ 0 & 0 & 0 & 0 & 0 & 1-2\nu_k \end{bmatrix} \tag{5}$$

For the individual material phases studied in this paper, subindex k can refer to either the unit inclusions u or the mortar joint matrix j.

According to the classic Reuss scheme, also referred to as isostress or inverse rule of mixtures, the expression of the stiffness tensor of the composite $\widehat{C}_m^V$ is a function of the stiffness tensors of the matrix C_j and the inclusions C_u and of their respective volume fractions ω_j and ω_u as follows:

$$\widehat{C}_m^R = \left(\omega_j C_j^{-1} + \omega_u C_u^{-1}\right)^{-1} \tag{6}$$

This approach neglects the influence of the Poisson's ratios of the material phases on the volumetric stiffness of the composite. Taking into account the Poisson's ratios of the phases, the resulting composite is transversely isotropic with a Young's modulus E_m^R in the principal direction and Poisson's ratio ν_m^R of the composite perpendicular to the principal direction. These parameters are calculated as [24]:

$$E_m^R = \frac{E_j E_u \left(\omega_j(1-\nu_u)E_j + \omega_u(1-\nu_j)E_u\right)}{E_j E_u\left(\omega_j^2(1-\nu_u) + \omega_u^2(1-\nu_j)\right) + \omega_j\omega_u\left((1+\nu_u)(1-2\nu_u)E_j^2 + 4\nu_j\nu_u E_j E_u + (1+\nu_j)(1-2\nu_j)E_u^2\right)}$$

$$\nu_m^R = \frac{E_j E_u \left(\omega_j(1-\nu_u)\nu_j + \omega_u(1-\nu_j)\omega_u\right)}{E_j E_u\left(\omega_j^2(1-\nu_u) + \omega_u^2(1-\nu_j)\right) + \omega_j\omega_u\left((1+\nu_u)(1-2\nu_u)E_j^2 + 4\nu_j\nu_u E_j E_u + (1+\nu_j)(1-2\nu_j)E_u^2\right)} \tag{7}$$

Substituting the values obtained from Eq. (7) into eq. (5) we obtain the tensor $\widetilde{C}_m^R$. The final enhanced expression of the Reuss stiffness tensor C_m^R for the composite is calculated as:

$$C_m^R = \begin{bmatrix} \widetilde{C}_m^R(1,1) & \widetilde{C}_m^R(1,2) & \widetilde{C}_m^R(1,3) & 0 & 0 & 0 \\ \widetilde{C}_m^R(2,1) & \widetilde{C}_m^R(2,2) & \widetilde{C}_m^R(2,3) & 0 & 0 & 0 \\ \widetilde{C}_m^R(3,1) & \widetilde{C}_m^R(3,2) & \widetilde{C}_m^R(3,3) & 0 & 0 & 0 \\ 0 & 0 & 0 & \widehat{C}_m^R(4,4) & 0 & 0 \\ 0 & 0 & 0 & 0 & \widehat{C}_m^R(5,5) & 0 \\ 0 & 0 & 0 & 0 & 0 & \widehat{C}_m^R(6,6) \end{bmatrix} \tag{8}$$

with the two indices in parentheses corresponding to the lines and columns respectively of the indicated tensors. According to eq. (8), in the enhanced expression of the stiffness tensor according to the Reuss scheme, the normal stiffness includes the influence of the Poisson's ratios of the material phases, leading to a more realistic representation of their mechanical interaction, while the shear stiffness is calculated as per the classic approach.

Similarly, according to the classic Voigt scheme, also known as isostrain or rule of mixtures, the stiffness tensor of the composite $\widehat{C}_m^V$ is calculated as follows:

$$\widehat{C}_m^V = \omega_j C_j + \omega_u C_u \tag{9}$$

The Young's modulus E_m^V in the principal direction and Poisson's ratio ν_m^V of the composite perpendicular to the principal direction taking into account the Poisson's ratios are equal to [24]:

$$E_m^V = \frac{\left(\omega_j(1-\nu_u)E_j + \omega_u(1-\nu_j)E_j\right)\left(\omega_j(1+\nu_u)E_j + \omega_u(1+\nu_j)E_u\right)}{\left(\omega_j(1-\nu_u^2)E_j + \omega_u(1-\nu_j^2)E_u\right)}$$

$$\nu_m^V = \frac{\omega_j\nu_j(1-\nu_u^2)E_j + \omega_u\nu_u\left(1-\nu_j^2\right)E_u}{\left(\omega_j(1-\nu_u^2)E_j + \omega_u(1-\nu_j^2)E_u\right)} \tag{10}$$

Substituting the values obtained from Eqn 10 to eq. (5) the tensor $\widetilde{C}_m^V$ is obtained. The final expression of the composite stiffness tensor C_m^R according to the enhanced Voigt approach is:

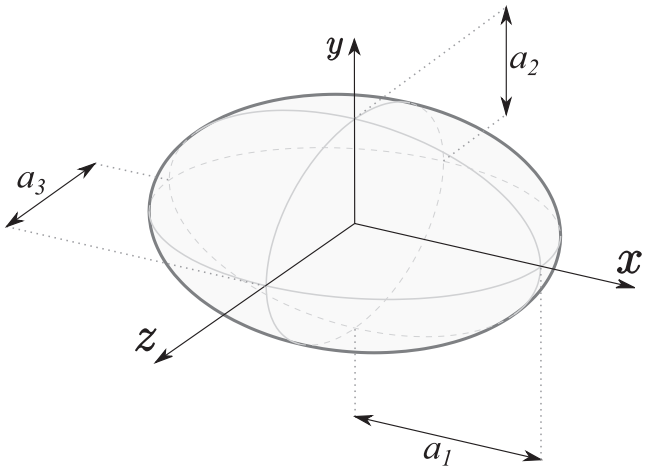

Fig. 6. Ellipsoidal inclusion in three-dimensional space with half-lengths indicated.

Table 4
Parameters used in parametric analysis.

Parameter	Range	Reference value
h_u	$0.35 \div 0.78\ t_u$	$0.52\ t_u$
$l_j = h_j = t_j$	$0.05 \div 0.20\ t_u$	$0.10\ t_u$
E_j	$0.001 \div 10\ E_u$	$0.1\ E_u$
$\nu_u = \nu_j$	0.15	0.15

$$C_m^V = \begin{bmatrix} \widetilde{C}_m^V(1,1) & \widetilde{C}_m^V(1,2) & \widetilde{C}_m^V(1,3) & 0 & 0 & 0 \\ \widetilde{C}_m^V(2,1) & \widetilde{C}_m^V(2,2) & \widetilde{C}_m^V(2,3) & 0 & 0 & 0 \\ \widetilde{C}_m^V(3,1) & \widetilde{C}_m^V(3,2) & \widetilde{C}_m^V(3,3) & 0 & 0 & 0 \\ 0 & 0 & 0 & \widehat{C}_m^V(4,4) & 0 & 0 \\ 0 & 0 & 0 & 0 & \widehat{C}_m^V(5,5) & 0 \\ 0 & 0 & 0 & 0 & 0 & \widehat{C}_m^V(6,6) \end{bmatrix} \tag{11}$$

According to the dilute inclusion approach to micromechanics [15],

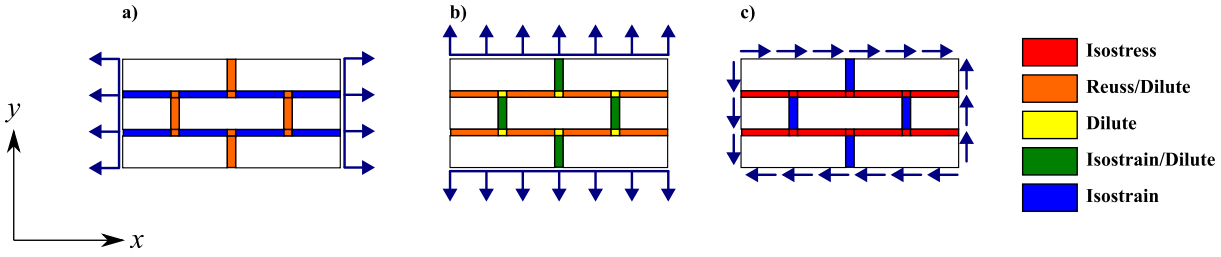

Fig. 7. Illustration of stress–strain conditions and combinations thereof for mortar joints in a staggered masonry bond pattern: a) applied strain in *xx* direction, b) applied strain in *yy* direction, c) applied strain in *xy* plane.

Table 3
Participation factors $P_{ab}^{c,n}$ for each joint type *n* for loading in the direction *ab* in stress–strain condition *c* for the masonry typologies investigated.

Bond	Joint type *n*	$P_{xx}^{R,n}/P_{xx}^{V,n}/P_{xx}^{MT,n}$	$P_{yy}^{R,n}/P_{yy}^{V,n}/P_{yy}^{MT,n}$	$P_{zz}^{R,n}/P_{zz}^{V,n}/P_{zz}^{MT,n}$	$P_{yz}^{R,n}/P_{yz}^{V,n}/P_{yz}^{MT,n}$	$P_{xz}^{R,n}/P_{xz}^{V,n}/P_{xz}^{MT,n}$	$P_{xy}^{R,n}/P_{xy}^{V,n}/P_{xy}^{MT,n}$
SB	Bed	0.0/1.0/0.0	1.0/0.0/0.0	0.0/1.0/0.0	1.0/0.0/0.0	0.0/1.0/0.0	1.0/0.0/0.0
	Cross	1.0/0.0/0.0	1.0/0.0/0.0	0.0/1.0/0.0	1.0/0.0/0.0	1.0/0.0/0.0	1.0/0.0/0.0
	Head	1.0/0.0/0.0	0.0/0.5/0.5	0.0/1.0/0.0	0.0/1.0/0.0	1.0/0.0/0.0	1.0/0.0/0.0
	Transversal	0.0/0.0/0.0	0.0/0.0/0.0	0.0/0.0/0.0	0.0/0.0/0.0	0.0/0.0/0.0	0.0/0.0/0.0
RB	Bed	0.0/1.0/0.0	0.5/0.0/0.5	0.0/1.0/0.0	1.0/0.0/0.0	0.0/1.0/0.0	1.0/0.0/0.0
	Cross	0.5/0.0/0.5	0.0/0.0/1.0	0.0/1.0/0.0	1.0/0.0/0.0	0.5/0.5/0.0	1.0/0.0/0.0
	Head	0.5/0.0/0.5	0.0/0.5/0.5	0.0/1.0/0.0	0.0/1.0/0.0	0.5/0.5/0.0	0.5/0.5/0.0
	Transversal	0.0/0.0/0.0	0.0/0.0/0.0	0.0/0.0/0.0	0.0/0.0/0.0	0.0/0.0/0.0	0.0/0.0/0.0
EB/FB	Bed	0.0/0.5/0.5	0.5/0.0/0.5	0.0/0.5/0.5	1.0/0.0/0.0	0.0/1.0/0.0	1.0/0.0/0.0
	Cross	0.0/0.5/0.5	0.5/0.0/0.5	0.0/0.5/0.5	1.0/0.0/0.0	0.5/0.5/0.0	1.0/0.0/0.0
	Head	0.5/0.0/0.5	0.0/0.5/0.5	0.0/0.5/0.5	0.0/1.0/0.0	0.5/0.5/0.0	0.5/0.5/0.0
	Transversal	0.0/0.5/0.5	0.0/1.0/0.0	0.5/0.0/0.5	0.5/0.0/0.5	1.0/0.0/0.0	0.0/0.0/1.0

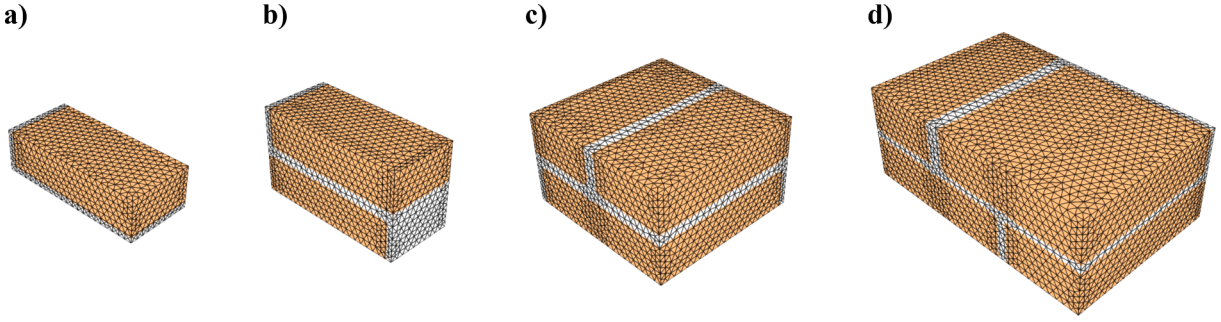

Fig. 8. Finite element meshes of periodic unit cells: a) stack, b) running, c) English and d) Flemish bond.

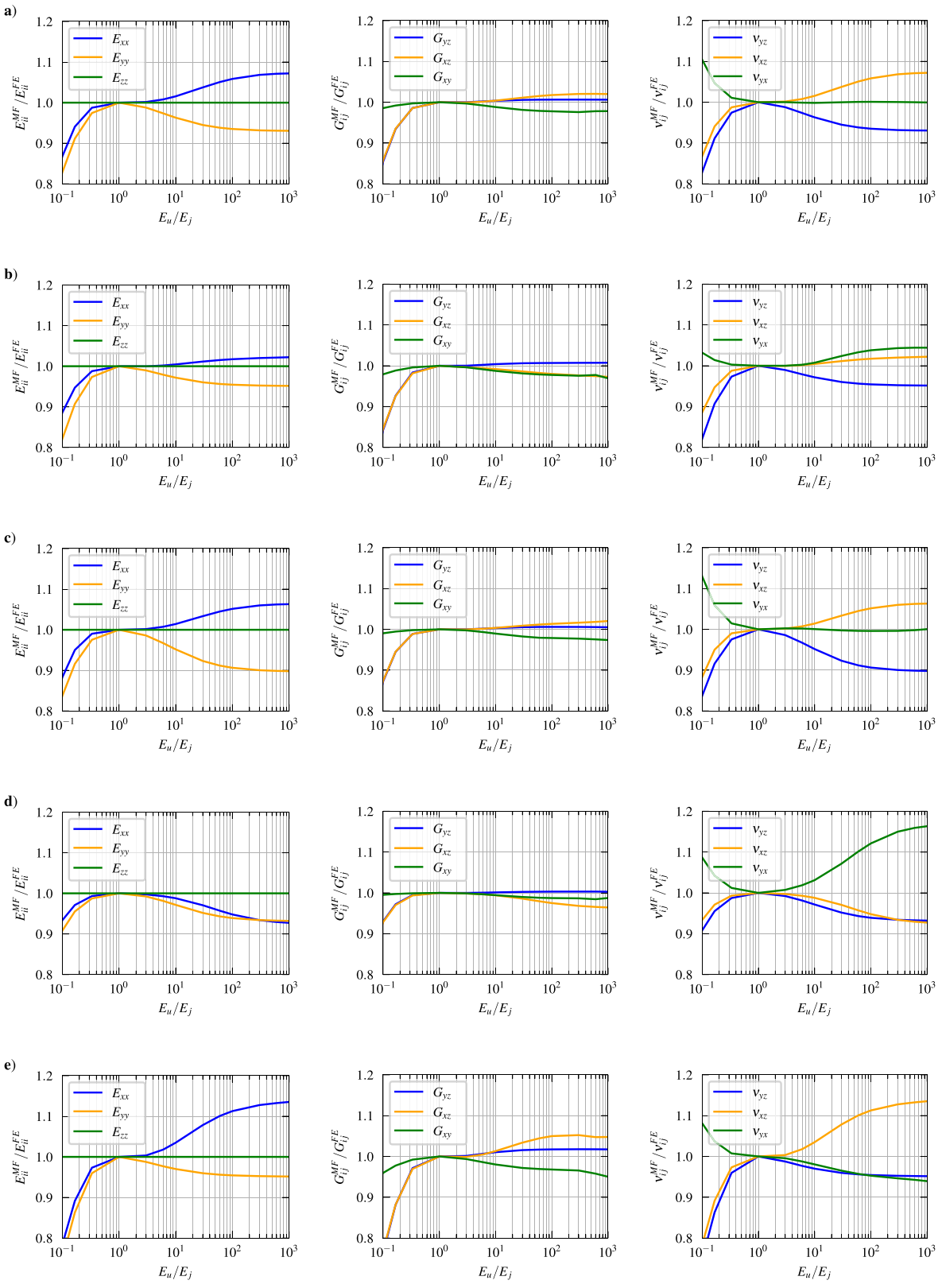

Fig. 9. Results of parametric analysis for stack bond masonry: a) reference, b) $h_u = 0.35t_u$, c) $h_u = 0.78t_u$, d) $l_j = h_j = t_j = 0.05t_u$, e).$l_j = h_j = t_j = 0.20t_u$

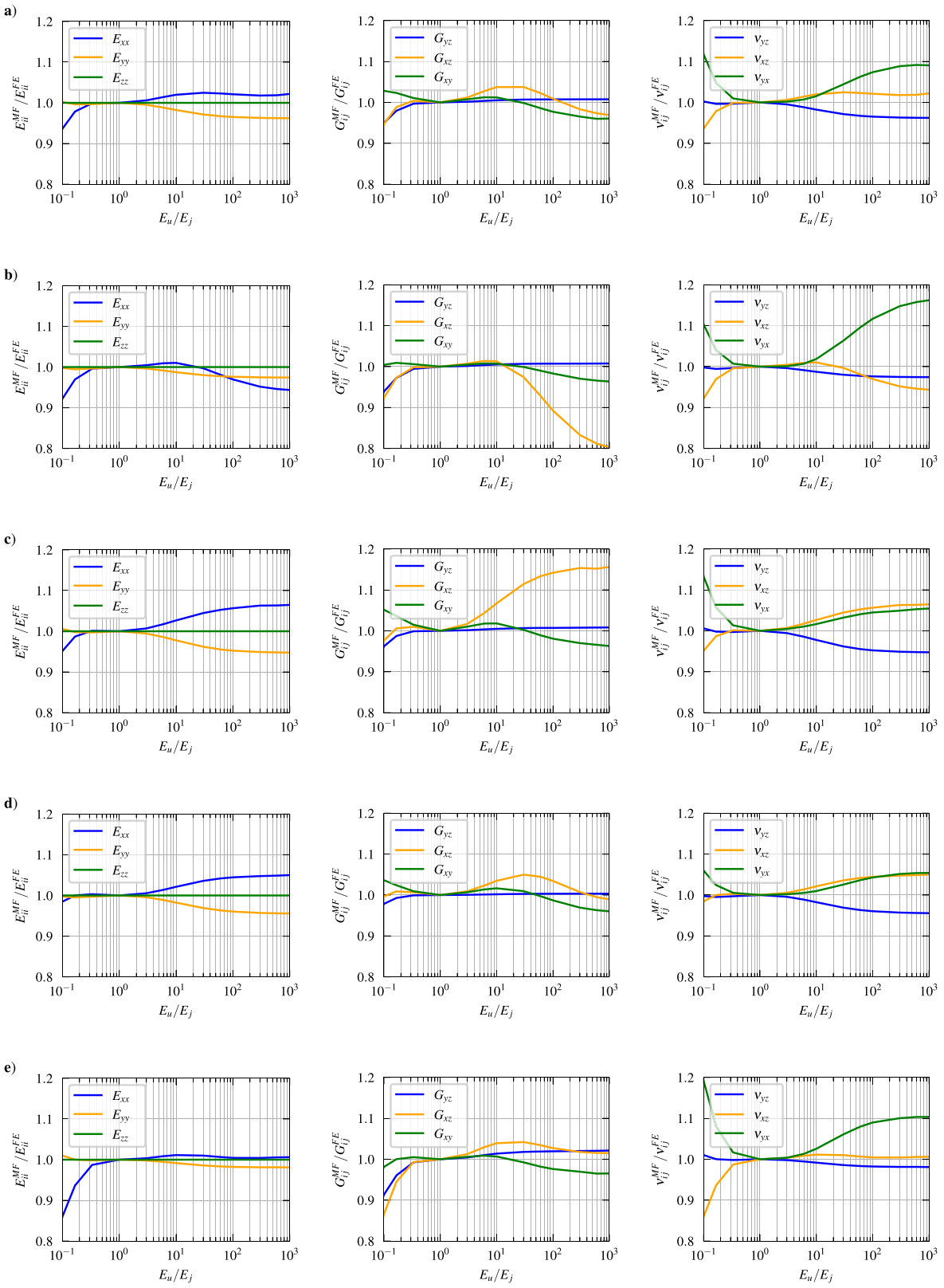

Fig. 10. Results of parametric analysis for running bond masonry: a) reference, b) $h_u = 0.35t_u$, c) $h_u = 0.78t_u$, d) $l_j = h_j = t_j = 0.05t_u$, e) $l_j = h_j = t_j = 0.20t_u$.

a single inhomogeneity is embedded in an infinite, homogeneous and isotropic matrix. Assuming that the matrix and the inclusion have different elastic properties, an applied strain in the matrix causes a different strain in the inclusion. The eigenstrain ε^* is defined as the strain state within the inclusion upon removal of the constraint provided to it by the surrounding matrix. As such, the components of the strain within the inclusion itself are equal to:

$$\varepsilon_{ij} = S_{ijkl}\varepsilon^*_{kl} \tag{12}$$

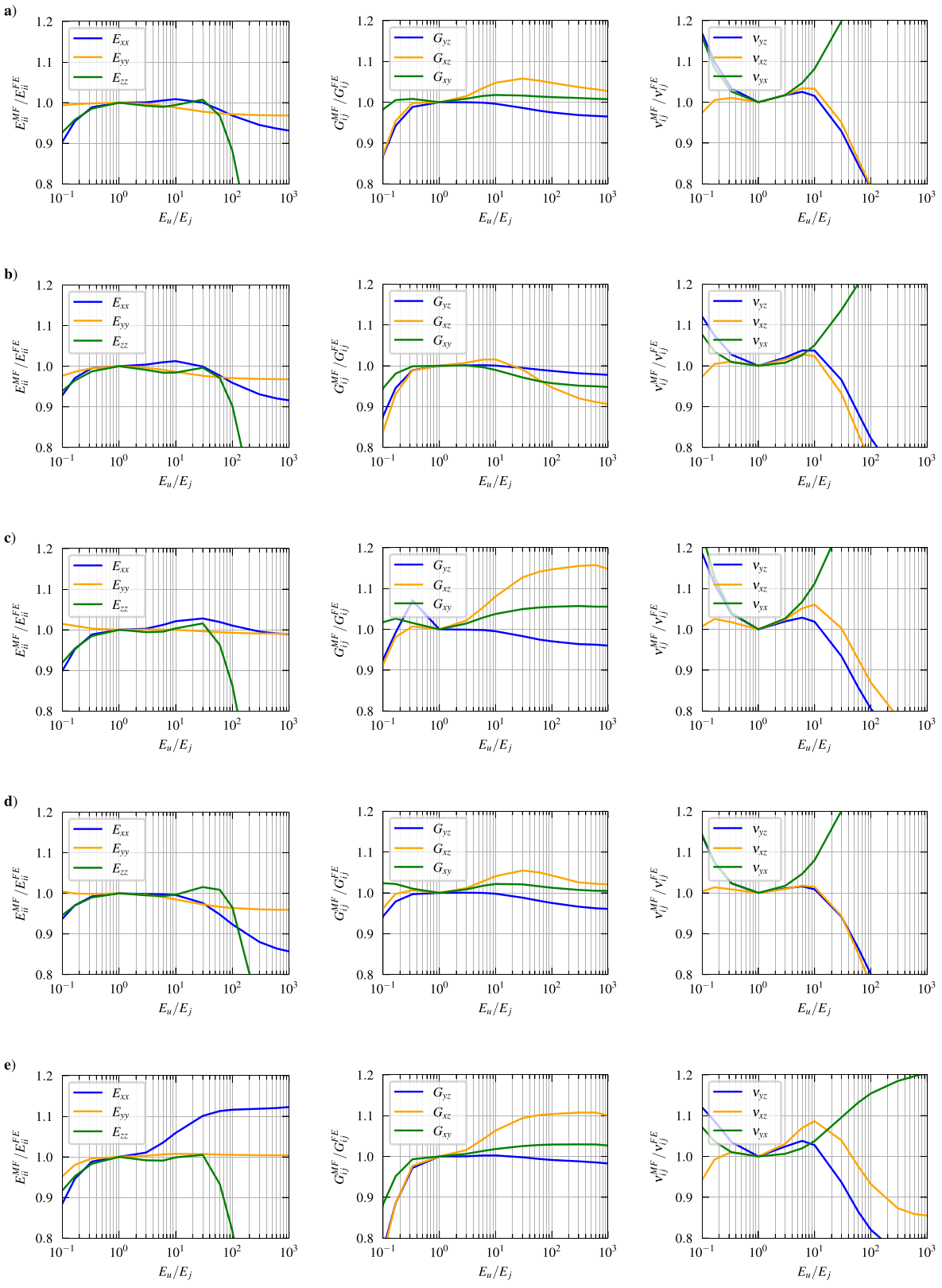

Fig. 11. Results of parametric analysis for English bond masonry: a) reference, b) $h_u = 0.35t_u$, c) $h_u = 0.78t_u$, d) $l_j = h_j = t_j = 0.05t_u$, e) $l_j = h_j = t_j = 0.20t_u$.

Table 5
Results of parametric analysis for reference values. Average value in parentheses.

Bond	$\widehat{E}_{xx}$	$\widehat{E}_{yy}$	$\widehat{E}_{zz}$	$\widehat{G}_{xy}$	$\widehat{G}_{xz}$	$\widehat{G}_{yz}$	$\widehat{\nu}_{xy}$	$\widehat{\nu}_{yx}$	$\widehat{\nu}_{xz}$	$\widehat{\nu}_{zx}$	$\widehat{\nu}_{yz}$	$\widehat{\nu}_{zy}$
SB	0.87÷1.07 (1.01)	0.83÷1 (0.94)	1÷1 (1)	0.98÷1 (0.99)	0.86÷1.02 (0.99)	0.85÷1.01 (0.99)	1÷1.16 (1.09)	1÷1.1 (1.01)	0.87÷1.07 (1.01)	1÷1 (1)	0.83÷1 (0.94)	1÷1 (1)
RB	0.94÷1.02 (1.01)	0.96÷1 (0.98)	1÷1 (1)	0.96÷1.03 (1)	0.95÷1.04 (1)	0.95÷1.01 (1)	1÷1.16 (1.08)	1÷1.12 (1.05)	0.94÷1.02 (1.01)	1÷1 (1)	0.96÷1 (0.98)	1÷1 (1)
EB	0.9÷1.01 (0.97)	0.97÷1 (0.98)	0.23÷1.01 (0.83)	0.98÷1.02 (1.01)	0.87÷1.06 (1.01)	0.87÷1 (0.97)	1÷1.4 (1.18)	1÷1.46 (1.2)	0.65÷1.03 (0.9)	0.16÷1.02 (0.8)	0.67÷1.17 (0.92)	0.16÷1.09 (0.81)
FB	0.92÷1.02 (0.99)	0.96÷1 (0.99)	0.27÷1.03 (0.85)	0.94÷1.03 (1.01)	0.87÷1.05 (1)	0.89÷1 (0.98)	1÷1.33 (1.15)	1÷1.33 (1.15)	0.54÷1.06 (0.88)	0.15÷1.03 (0.8)	0.58÷1.22 (0.92)	0.16÷1.16 (0.83)

Table 6
Results of parametric analysis for $h_u = 0.35t_u$. Average value in parentheses.

Bond	$\widehat{E}_{xx}$	$\widehat{E}_{yy}$	$\widehat{E}_{zz}$	$\widehat{G}_{xy}$	$\widehat{G}_{xz}$	$\widehat{G}_{yz}$	$\widehat{\nu}_{xy}$	$\widehat{\nu}_{yx}$	$\widehat{\nu}_{xz}$	$\widehat{\nu}_{zx}$	$\widehat{\nu}_{yz}$	$\widehat{\nu}_{zy}$
SB	0.89÷1.02 (0.99)	0.82÷1 (0.95)	1÷1 (1)	0.97÷1 (0.98)	0.85÷1 (0.97)	0.84÷1.01 (0.98)	1÷1.12 (1.07)	1÷1.04 (1.02)	0.89÷1.02 (0.99)	1÷1 (1)	0.82÷1 (0.95)	1÷1 (1)
RB	0.92÷1.01 (0.98)	0.97÷1 (0.99)	1÷1 (1)	0.96÷1.01 (0.99)	0.8÷1.01 (0.94)	0.94÷1.01 (1)	1÷1.13 (1.06)	1÷1.16 (1.07)	0.92÷1.01 (0.98)	1÷1 (1)	0.97÷1 (0.99)	1÷1 (1)
EB	0.92÷1.01 (0.97)	0.97÷1 (0.98)	0.26÷1 (0.84)	0.95÷1 (0.97)	0.84÷1.02 (0.96)	0.88÷1 (0.98)	1÷1.28 (1.12)	1÷1.35 (1.14)	0.61÷1.03 (0.88)	0.17÷1 (0.79)	0.69÷1.12 (0.93)	0.19÷1.08 (0.83)
FB	0.91÷1.01 (0.96)	0.96÷1 (0.99)	0.31÷1.02 (0.86)	0.91÷1 (0.99)	0.84÷1.02 (0.96)	0.89÷1 (0.98)	1÷1.22 (1.1)	1÷1.34 (1.14)	0.48÷1.04 (0.84)	0.16÷1.01 (0.79)	0.6÷1.19 (0.94)	0.19÷1.14 (0.85)

where S_{ijkl} are the components of Eshelby's tensor S. These components are a function of the shape and aspect ratio of the inclusions. In the present investigation ellipsoidal inclusions will be considered for the analysis of cuboidal masonry units, an assumption that has been demonstrated to be sufficiently accurate through comparison with experimental data [4]. The expression defining the outer surface of an ellipsoid is:

$$\frac{x^2}{{a_1}^2}+\frac{y^2}{{a_2}^2}+\frac{z^2}{{a_3}^2}=1 \tag{13}$$

where a_1, a_2 and a_3 are the half-length, half-height and half-width of the ellipsoid respectively along the x, y and z axes, as shown in Figure 6.

The form of Eshelby's tensor S is:

$$S=\begin{bmatrix} S_{1111} & S_{1122} & S_{1133} & 0 & 0 & 0 \\ S_{2211} & S_{2222} & S_{2233} & 0 & 0 & 0 \\ S_{3311} & S_{3322} & S_{3333} & 0 & 0 & 0 \\ 0 & 0 & 0 & S_{2323} & 0 & 0 \\ 0 & 0 & 0 & 0 & S_{1313} & 0 \\ 0 & 0 & 0 & 0 & 0 & S_{1212} \end{bmatrix} \tag{14}$$

The components of the tensor in the case of ellipsoidal inclusions are calculated as follows[28]:

$$S_{1111}=\frac{3}{8\pi(1-\nu_j)}{a_1}^2 I_{11}+\frac{1-2\nu_j}{8\pi(1-\nu_j)}I_1$$

$$S_{1122}=\frac{1}{8\pi(1-\nu_j)}{a_2}^2 I_{12}+\frac{1-2\nu_j}{8\pi(1-\nu_j)}I_1$$

$$S_{1133}=\frac{1}{8\pi(1-\nu_j)}{a_3}^2 I_{13}+\frac{1-2\nu_j}{8\pi(1-\nu_j)}I_1$$

$$S_{1212}=\frac{{a_1}^2+{a_2}^2}{16\pi(1-\nu_j)}I_{12}+\frac{1-2\nu_j}{16\pi(1-\nu_j)}(I_1+I_2) \tag{15}$$

where ν_j is the Poisson's ratio of the matrix. The parameters I_i and I_{ij} are calculated according to the elliptical integrals [32]:

$$I_1=2\pi a_1 a_2 a_3\int_0^\infty \frac{\mathrm{d}s}{({a_1}^2+s)\Delta(s)}$$

$$I_{11}=2\pi a_1 a_2 a_3\int_0^\infty \frac{\mathrm{d}s}{({a_1}^2+s)^2\Delta(s)}$$

$$I_{12}=2\pi a_1 a_2 a_3\int_0^\infty \frac{\mathrm{d}s}{({a_1}^2+s)({a_2}^2+s)\Delta(s)} \tag{16}$$

with:

$$\Delta(s)=\sqrt{({a_1}^2+s)({a_2}^2+s)({a_3}^2+s)} \tag{17}$$

The remaining parameters I_i and I_{ij} are calculated by cyclic permutation through subscripts $1, 2, 3$.

For an elliptical cylinder inclusion infinitely long in the transversal direction ($a_3 \to \infty$), the components of Eshelby's tensor S are simplified to the following expressions [4]:

$$S_{1111}=\frac{a}{2(1-\nu_j)}\left(\frac{2+a}{(1+a)^2}+\frac{1-2\nu_j}{1+a}\right)$$

$$S_{1122}=\frac{a}{2(1-\nu_j)}\left(\frac{a}{(1+a)^2}-\frac{1-2\nu_j}{1+a}\right)$$

$$S_{1133}=\frac{\nu_j}{1-\nu_j}\frac{a}{1+a}$$

$$S_{2211}=\frac{1}{2(1-\nu_j)}\left(\frac{1}{(1+a)^2}-\frac{1-2\nu_j}{1+a}\right)$$

$$S_{2222}=\frac{1}{2(1-\nu_j)}\left(\frac{1+2a}{(1+a)^2}+\frac{1-2\nu_j}{1+a}\right)$$

Table 7
Results of parametric analysis for $h_{ul} = 0.78t_u$. Average value in parentheses.

Bond	$\widehat{E}_{xx}$	$\widehat{E}_{yy}$	$\widehat{E}_{zz}$	$\widehat{G}_{xy}$	$\widehat{G}_{xz}$	$\widehat{G}_{yz}$	$\widehat{\nu}_{xy}$	$\widehat{\nu}_{yx}$	$\widehat{\nu}_{xz}$	$\widehat{\nu}_{zx}$	$\widehat{\nu}_{yz}$	$\widehat{\nu}_{zy}$
SB	0.88÷1.06 (1.01)	0.84÷1 (0.93)	1÷1 (1)	0.97÷1 (0.99)	0.87÷1.02 (0.99)	0.87÷1.01 (0.99)	1÷1.19 (1.11)	1÷1.13 (1.01)	0.88÷1.06 (1.01)	1÷1 (1)	0.84÷1 (0.93)	1÷1 (1)
RB	0.95÷1.06 (1.03)	0.95÷1.01 (0.97)	1÷1 (1)	0.96÷1.05 (1)	0.98÷1.16 (1.07)	0.96÷1.01 (1)	1÷1.18 (1.09)	1÷1.13 (1.04)	0.95÷1.06 (1.03)	1÷1 (1)	0.95÷1.01 (0.97)	1÷1 (1)
EB	0.9÷1.03 (0.99)	0.99÷1.01 (1)	0.21÷1.02 (0.83)	1÷1.06 (1.04)	0.91÷1.16 (1.07)	0.93÷1.07 (0.98)	1÷1.58 (1.25)	1÷1.58 (1.26)	0.74÷1.06 (0.94)	0.16÷1.04 (0.81)	0.69÷1.19 (0.93)	0.15÷1.07 (0.8)
FB	0.92÷1.06 (1.02)	0.99÷1.02 (1.01)	0.25÷1.04 (0.85)	0.97÷1.11 (1.04)	0.9÷1.09 (1.04)	0.94÷1.02 (0.99)	1÷1.47 (1.21)	1÷1.43 (1.2)	0.63÷1.1 (0.93)	0.15÷1.06 (0.81)	0.61÷1.25 (0.93)	0.15÷1.14 (0.83)

$$S_{2233} = \frac{\nu_j}{1-\nu_j}\frac{1}{1+a}$$

$$S_{3311} = S_{3322} = S_{3333} = 0$$

$$S_{2323} = \frac{1}{2(1-a)}$$

$$S_{1313} = \frac{a}{2(1-a)}$$

$$S_{1212} = \frac{a}{4(1-\nu_j)}\left(\frac{1+a^2}{(1+a)^2} - (1-2\nu_j)\right) \tag{18}$$

with $a = a_2/a_1$ being the aspect ratio of the inclusion.

In the Mori-Tanaka scheme, different families of inclusions can be considered for the calculation of the stiffness tensor of the composite material. In this context, the dilute estimate of the strain concentration tensor for the i-th inclusion family embedded in the matrix j is calculated as:

$$T_i = \left(I + S_i\left(C_j\right)^{-1}\left(C_i - C_j\right)\right)^{-1} \tag{19}$$

where I is the 6×6 identity tensor and S_i is Eshelby's tensor as defined for the i-th inclusion family according to eq. (14).

The strain concentration factor of the matrix j with different embedded inclusion families is equal to:

$$A_j = \left(\omega_j I + \sum_i \omega_i T_i\right)^{-1} \tag{20}$$

where ω_i is the volume fraction of the i-th inclusion family within the composite.

The strain concentration tensor for the i-th inclusion family is equal to:

$$A_i = T_i A_j \tag{21}$$

Finally, the stiffness tensor of the composite according to the Mori-Tanaka scheme is equal to:

$$C_m^{MT} = C_j + \sum_i \omega_i\left(C_i - C_j\right)A_i \tag{22}$$

3.3. Combination of the stress–strain conditions

The final expression of the stiffness tensor of the composite C_m^{MF} was a combination of the Reuss (R), Voigt (V) and Mori-Tanaka (MT) mean-field homogenisation stiffness tensors (eq. (8), eq. (11) and eq. (22) respectively) according to the equation:

$$C_m^{MF} = \left(I_R C_m^{R\,-1} + I_V C_m^{V\,-1} I_{MT} C_m^{MT\,-1}\right)^{-1} \tag{23}$$

where I_R, I_V and I_{MT} are diagonal weighing tensors expressing the contribution of each stress–strain condition to the mechanical response of the composite. These weighing tensors contain the relative volume ratio of the matrix understood to be participating in each of the stress–strain conditions (R, V or MT) for each direction or plane of loading (xx, yy, zz, yz, xz or xy). The weighted combination of mean-field homogenisation schemes as expressed in eq. (23) can be understood as an enhanced inverse rule of mixtures between the various stress–strain conditions involved in the response of the composite.

The weighing tensors assume the following diagonal form:

Table 8
Results of parametric analysis for $l_j = h_j = t_j = 0.05t_u$. Average value in parentheses.

Bond	$\widehat{E}_{xx}$	$\widehat{E}_{yy}$	$\widehat{E}_{zz}$	$\widehat{G}_{xy}$	$\widehat{G}_{xz}$	$\widehat{G}_{yz}$	$\widehat{\nu}_{xy}$	$\widehat{\nu}_{yx}$	$\widehat{\nu}_{xz}$	$\widehat{\nu}_{zx}$	$\widehat{\nu}_{yz}$	$\widehat{\nu}_{zy}$
SB	0.93÷1 (0.96)	0.91÷1 (0.96)	1÷1 (1)	0.98÷1 (0.99)	0.93÷1 (0.98)	0.93÷1 (0.99)	1÷1.16 (1.08)	1÷1.16 (1.07)	0.93÷1 (0.96)	1÷1 (1)	0.91÷1 (0.96)	1÷1 (1)
RB	0.98÷1.05 (1.02)	0.96÷1 (0.98)	1÷1 (1)	0.96÷1.04 (1)	0.99÷1.05 (1.02)	0.98÷1 (1)	1÷1.16 (1.08)	1÷1.06 (1.03)	0.98÷1.05 (1.02)	1÷1 (1)	0.96÷1 (0.98)	1÷1 (1)
EB	0.86÷1 (0.95)	0.96÷1 (0.98)	0.34÷1.02 (0.88)	1÷1.02 (1.01)	0.96÷1.05 (1.02)	0.94÷1 (0.98)	1÷1.43 (1.18)	1÷1.6 (1.23)	0.58÷1.02 (0.88)	0.23÷1.02 (0.83)	0.63÷1.14 (0.91)	0.22÷1.07 (0.84)
FB	0.89÷1 (0.96)	0.97÷1 (0.99)	0.38÷1.04 (0.9)	1÷1.03 (1.02)	0.94÷1.04 (0.99)	0.95÷1 (0.99)	1÷1.35 (1.16)	1÷1.49 (1.19)	0.46÷1.04 (0.86)	0.57÷1.24 (0.91)	0.52÷1.18 (0.9)	0.2÷1.12 (0.85)

Table 9
Results of parametric analysis for $l_j = h_j = t_j = 0.20t_u$. Average value in parentheses.

Bond	$\widehat{E}_{xx}$	$\widehat{E}_{yy}$	$\widehat{E}_{zz}$	$\widehat{G}_{xy}$	$\widehat{G}_{xz}$	$\widehat{G}_{yz}$	$\widehat{\nu}_{xy}$	$\widehat{\nu}_{yx}$	$\widehat{\nu}_{xz}$	$\widehat{\nu}_{zx}$	$\widehat{\nu}_{yz}$	$\widehat{\nu}_{zy}$
SB	0.78÷1.14 (1.03)	0.75÷1 (0.94)	1÷1 (1)	0.95÷1 (0.97)	0.77÷1.05 (0.99)	0.76÷1.02 (0.98)	1÷1.13 (1.07)	0.94÷1.08 (0.98)	0.78÷1.14 (1.03)	1÷1 (1)	0.75÷1 (0.94)	1÷1 (1)
RB	0.86÷1.01 (0.99)	0.98÷1.01 (0.99)	1÷1 (1)	0.96÷1.01 (0.99)	0.87÷1.04 (1)	0.91÷1.02 (1)	1÷1.13 (1.06)	1÷1.19 (1.07)	0.86÷1.01 (0.99)	1÷1 (1)	0.98÷1.01 (0.99)	1÷1 (1)
EB	0.88÷1.12 (1.05)	0.95÷1.01 (1)	0.19÷1 (0.81)	0.88÷1.03 (1)	0.76÷1.11 (1.03)	0.77÷1 (0.97)	1÷1.35 (1.15)	1÷1.21 (1.09)	0.86÷1.09 (0.97)	0.14÷1.02 (0.79)	0.74÷1.12 (0.94)	0.14÷1.08 (0.79)
FB	0.9÷1.18 (1.07)	0.91÷1.02 (1)	0.23÷1.04 (0.84)	0.84÷1.06 (1.01)	0.76÷1.09 (1.02)	0.8÷1.01 (0.98)	1÷1.27 (1.12)	1÷1.11 (1.05)	0.74÷1.11 (0.95)	0.14÷1.04 (0.79)	0.66÷1.15 (0.93)	0.15÷1.14 (0.83)

$$I^c = \begin{bmatrix} \widehat{\omega}^c_{xx} & 0 & 0 & 0 & 0 & 0 \\ 0 & \widehat{\omega}^c_{yy} & 0 & 0 & 0 & 0 \\ 0 & 0 & \widehat{\omega}^c_{zz} & 0 & 0 & 0 \\ 0 & 0 & 0 & \widehat{\omega}^c_{yz} & 0 & 0 \\ 0 & 0 & 0 & 0 & \widehat{\omega}^c_{xz} & 0 \\ 0 & 0 & 0 & 0 & 0 & \widehat{\omega}^c_{xy} \end{bmatrix} \tag{24}$$

where the superscript c indicates the stress–strain condition with $c = \{R, V, MT\}$, the subscripts (xx, yy, etc.) indicate the direction or plane of the load and $\widehat{\omega}$ indicates the relative volume ratio of the matrix participating in the load condition. For example, $\widehat{\omega}^R_{xx}$ indicates the relative volume ratio of the matrix participating in the composite under Reuss stress–strain conditions for a macroscopic stress applied on the composite in the xx direction.

Each parameter $\widehat{\omega}^c_{ab}$ is calculated as:

$$\widehat{\omega}^c_{ab} = \sum_n P^{c,n}_{ab} \widehat{\omega}_n \tag{25}$$

with $n = \{b, c, h, t\}$ as defined in eq. (4) and $P^{c,n}_{ab}$ indicating participation factors in the c stress–strain condition. For example, $P^{R,b}_{yy} = 1.0$ means that the bed joint ($n = b$) participates entirely in the Reuss stress–strain condition ($c = R$) for macroscopic loading applied in the vertical direction ($ab = yy$). Naturally, the sum of participation factors in every joint n for a given loading direction ab needs to comply with $\sum_n P^{c,n}_{ab} = 1.0$.

3.4. Implementation

The homogenisation scheme was applied according to eq. (23) using the volume fractions shown in Table 2 for the different masonry bonds. Eshelby's tensor S is calculated according to the values given in eq. (18) for stretcher units in SB and RB masonry and for header units in EB and FB masonry. This is due to these units extending through the entire transversal thickness of the cell. Conversely, the parameters for Eshelby's tensor for stretcher units in EB and FB masonry are calculated according to eq. (15).

For clarifying the determination of participation factors $P^{c,n}_{ab}$, the stress–strain condition for each joint type in a staggered masonry bond pattern for different macroscopic strain loads is illustrated in Figure 7. For loading in the xx direction, the bed joints are in isostrain conditions due to their positioning between the beds of the units. Conversely, the head and cross joints are in an intermediate state between isostress and dilute conditions, the former due to their orientation with respect to the load direction and the latter due to the restriction of their deformation from the neighbouring unit bed. For loading in the yy direction, the bed joints are in isostress conditions due to their unrestricted deformation in the direction of the load, which is a consequence of the continuity of the bed joint. Conversely, the deformation of the head joints is restricted by the unit headers, resulting in a condition between isostrain and dilute. The cross joints are considered to be in a dilute condition. Finally, for loading in the xy plane, the continuity of the bed joints results in the bed and cross joints to be in isostress conditions, while the head joints are in isostrain conditions due to their position between the unit headers which restricts their deformation.

According to the above scheme, the resulting participation factors $P^{c,n}_{ab}$ used in eq. (25) presented in Table 3. As mentioned, the elected participation factors $P^{c,n}_{ab}$ reflect the stresses developed in a joint type for a given applied macroscopic stress. For instance, in the case of SB masonry, the head and cross joints are in isostress conditions for loading in xx, therefore $P^{R,c}_{xx} = P^{R,h}_{xx} = 1.0$. In the usual case of staggered interlocking of the stretcher units, such as that encountered in RB, EB and FB masonry, the head joints are only partially in isostress condition for the same horizontal loading case. This behaviour is reflected by introducing the contribution of a dilute condition by setting $P^{MT,h}_{xx} = 0.5$. Generally, when the stress–strain condition of a joint cannot be interpreted as being purely isostress or isostrain, a value of 0.5 is adopted for the most appropriate of these two conditions and 0.5 for the dilute condition. This semi-empirical approach allows the simultaneous representation of the stress–strain condition of the joint and its interaction with the unit inclusions embedded in the composite.

4. Model validation

4.1. Finite element benchmark comparison

The accuracy of the proposed homogenisation scheme was evaluated through comparison with results obtained from a finite element benchmark. Finite element models of masonry PUCs were generated and analysed using the FEniCS computing platform [3]. The finite element meshes were composed of quadratic tetrahedrons with a maximum length of 5 mm. Representative finite element meshes of the four masonry bonds are illustrated in Figure 8. The PUCs were subjected to 6 load cases, each consisting of a displacement applied to the external faces of the cell resulting in strain along each normal direction or shear plane ab, simultaneously complying with periodic boundary conditions at the opposing faces of the domain. The resulting macroscopic stress and strain components were calculated numerically within the volume of the cell according to the Hill-Mandel averages [20]:

$$\bar{\sigma}_{ab} = \frac{1}{V_c}\int_V \sigma_{ab} dV$$

$$\bar{\varepsilon}_{ab} = \frac{1}{V_c}\int_V \varepsilon_{ab} dV \tag{26}$$

Finally, the stiffness tensor of the composite material C^{FE}_m according to the finite element analysis is computed as:

$$C^{FE}_m = (\bar{\varepsilon})^{-1}\bar{\sigma} \tag{27}$$

where $\bar{\sigma}$ and $\bar{\varepsilon}$ are the average strain and stress vectors.

A parametric analysis was performed in order to obtain a wide array of results for each bond type. The dimension and material parameters used are presented in a normalised format in Table 4. The width t_u and the Young's modulus E_u of the units were kept constant, while small adjustments were made to the length of the units l_u for maintaining

Table 10
Results of parametric analysis using plain Mori-Tanaka scheme for reference values. Average value in parentheses.

Bond	$\widehat{E}_{xx}$	$\widehat{E}_{yy}$	$\widehat{E}_{zz}$	$\widehat{G}_{xy}$	$\widehat{G}_{xz}$	$\widehat{G}_{yz}$	$\widehat{\nu}_{xy}$	$\widehat{\nu}_{yx}$	$\widehat{\nu}_{xz}$	$\widehat{\nu}_{zx}$	$\widehat{\nu}_{yz}$	$\widehat{\nu}_{zy}$
SB	1÷1.5 (1.2)	0.96÷1 (0.98)	0.01÷1 (0.51)	1÷2.89 (1.96)	1÷1.34 (1.14)	1÷2.08 (1.56)	1÷2.32 (1.55)	1÷1.49 (1.24)	1÷133.89 (22.19)	1÷1.23 (1.11)	1÷119.36 (20.17)	1÷1.71 (1.38)
RB	1÷1.14 (1.06)	0.97÷1.13 (1)	0.01÷1 (0.51)	1÷2.57 (1.83)	0.75÷1.03 (0.92)	1÷2.09 (1.58)	1÷2.33 (1.54)	1÷1.98 (1.42)	1÷101.67 (17.2)	1÷1.23 (1.11)	1÷119.53 (20.23)	1÷1.71 (1.38)
EB	0.91÷1 (0.97)	0.81÷1.02 (0.9)	0.04÷1 (0.62)	1÷2.12 (1.63)	1÷1.49 (1.24)	1÷1.93 (1.51)	1÷2.63 (1.71)	1÷2.33 (1.56)	1÷32.36 (6.27)	1÷1.58 (1.26)	1÷38.16 (7.2)	1÷2.1 (1.51)
FB	0.97÷1.01 (0.99)	0.81÷1 (0.9)	0.05÷1 (0.62)	1÷2.15 (1.63)	1÷1.46 (1.23)	1÷1.94 (1.52)	1÷2.55 (1.68)	1÷2.12 (1.48)	1÷27.6 (5.57)	1÷1.55 (1.26)	1÷31.95 (6.31)	1÷2.16 (1.55)

conformity with the condition expressed in eq. (1). Changes in the height of the units h_u and the thickness of the joints $l_j = h_j = t_j$ were applied individually. Conversely, the entire range of values for the Young's modulus of the mortar E_j was applied for each modification instance of the geometric parameters. The range of the ratio of Young's moduli of units and mortar E_u/E_j reflects the realistically expected range for the relative elastic stiffness of the material phases (namely $E_u/E_j = 0.1 \div 10$). Additionally, the range also extends to relative stiffness in the case of yielding of the mortar, at which point the ratio tends to infinity due to loss of stiffness in the mortar ($E_u/E_j \rightarrow +\infty$) [39].

The results of the parametric analysis are presented in Figure 9 through Figure 12. The horizontal axis in all graphs indicates the variation of the E_u/E_j ratio while the vertical axes indicate the ratio between the value of an elastic modulus E_{ii}, G_{ij} or Poisson's ratio ν_{ij} calculated using the proposed model over the value calculated through finite element analysis. An ordinate equal to 1.0 in the graphs indicates equality between the predictions of the scheme and the finite element analysis result. The Young's moduli were predicted with good accuracy for the majority of the cases, with accuracy being lost for a stiffness ratio approaching $E_u/E_j \rightarrow 0.1$ for SB and for RB with $l_j = h_j = t_j = 0.20t_u$. Similarly, the Young's moduli predictions lost accuracy for a stiffness ratio approaching $E_u/E_j \rightarrow 1000$ for SB, EB and FB with $l_j = h_j = t_j = 0.20t_u$. While the transversal Young's modulus E_{zz} was predicted with excellent accuracy for SB and RB, which are single-wythe typologies, the model underestimated the stiffness in the EB and FB cases for $E_u/E_j > 100$. However, normal macroscopic stresses are typically not applied transversally on masonry walls in buildings, thus reducing the practical impact of this discrepancy in the prediction. The shear moduli were overall predicted with good accuracy with a few exceptions, such as RB and EB with $h_u = 0.78\ t_u$. Finally, there were inaccuracies in the prediction of the Poisson's ratios for $E_u/E_j > 100$, mostly notable in the double-wythe EB and FB cases. Overall, the proposed model presented higher accuracy for cases where the units are stiffer than the mortar, which represents the vast majority of masonry construction made with solid brick and stone units.

The results of the parametric analysis are also summarised in Table 5 through Table 9. The accuracy of the prediction of the elastic properties is presented in terms of the minimum, maximum and average of the ratio of the proposed scheme prediction value over the finite element result. This ratio is symbolised as $\widehat{E}_{ii}$, $\widehat{E}_{ij}$ or $\widehat{\nu}_{ij}$ for the Young's moduli, shear moduli and Poisson's ratios respectively. The average was calculated disregarding the trivial case of $E_u/E_j = 1.0$. All Young's and shear modulus predictions presented excellent accuracy in terms of the average, apart from the aforementioned discrepancy in the transversal stiffness prediction in the EB and FB cases.

4.2. Comparison with other mean-field models

A comparison of the results between the proposed scheme and the plain Mori-Tanaka (*MT*) scheme for the reference values is presented in Table 10. This scheme produces the most realistic results among the three classical homogenisation schemes considered in this paper, as the Reuss scheme typically results in too low stiffness while Voigt results in too high stiffness. The proposed mixed model was notably more accurate in terms of predicted horizontal, vertical and especially transversal stiffness compared to the plain *MT* scheme. Conversely, the proposed scheme was substantially more accurate in the prediction of all shear moduli and the Poisson's ratios. A further important weakness of the plain *MT* scheme is that its predictions for the SB and RB cases are identical due to them having the same mortar volume fraction ω_j. This feature is resolved in the proposed scheme, which takes into account the bonding pattern of the masonry and the geometrical arrangement of the joint types.

The *MT* results for the RB masonry are also visualised in Figure 13. While the *MT* scheme offers reasonable accuracy for E_{xx} and E_{yy}, especially for a stiffness ratio E_u/E_j between 0.1 and 10, it is particularly inaccurate in predicting the shear moduli, of which the in-plane E_{xy} is of the highest importance in shear walls, and the Poisson's ratios, which are substantially overestimated. Finally, the proposed model is more accurate than the plain *MT* scheme for $E_u/E_j \rightarrow 0.1$, thus proving superior to the classical *MT* scheme for the case of mortar with higher stiffness than the units.

Overall, the proposed scheme provided significant accuracy advantages compared to classical mean-field homogenisation techniques by taking into account the stress–strain conditions of different areas of the matrix, namely the joints, under different types of macroscopic loading.

Finally, the proposed scheme was compared with the results of recently elaborated mean-field homogenisation scheme based on an interpolation between different considerations for the behaviour of the inclusions [38]. The comparison was performed in terms of the mean absolute error of the predictions of the elastic properties of Flemish bind masonry in the range of $E_u/E_j = [1, 1000]$ and presented in Table 11. The proposed model provided an improvement in the accuracy of the prediction of the Young's and shear moduli. Conversely, the accuracy of the Poisson's ratios was reduced. However, the magnitude of the Poisson's ratios of the composite for which the proposed model loses accuracy is small (lower than 0.05), which reduces the impact of this inaccuracy in practical terms.

5. Conclusions

A mixed mean-field homogenisation scheme for various types of masonry bonding patterns was proposed. The scheme, based on the weighed combination of classical mean-field homogenisation schemes, is capable of taking into account the geometry and different stress–strain conditions at different joints in the masonry composite, thus overcoming the problem of loss of geometric information of the matrix in other mean-field homogenisation schemes, such as the Reuss, Voigt and dilute approaches. The scheme, due to its analytical nature and very low computational intensity, allows the analysis of large structural systems without resulting in excessive computational cost through implementation in a finite element macromodel context.

The scheme was verified against results from a finite element benchmark, providing very accurate results for a wide spectrum of material and geometrical parameters. The proposed model presents a substantial improvement in terms of accuracy compared to other mean-field homogenisation schemes while simultaneously not requiring computational resources for its implementation, thus being more attractive compared to computationally intensive finite element homogenisation approaches.

The scheme is primarily applicable in masonry with solid units and completely filled joints, and is primarily intended for structures

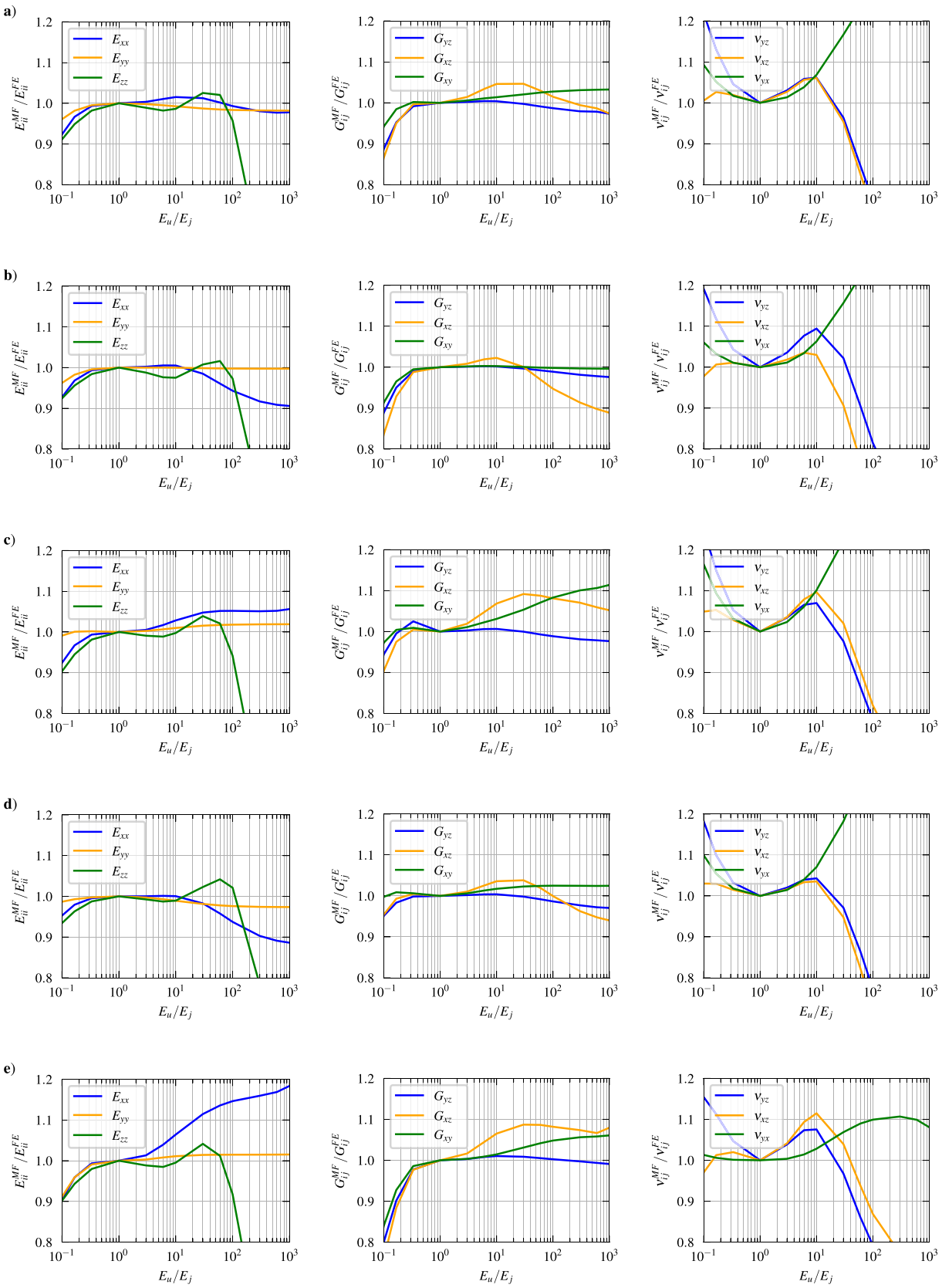

Fig. 12. Results of parametric analysis for Flemish bond masonry: a) reference, b) $h_u = 0.35t_u$, c) $h_u = 0.78t_u$, d) $l_j = h_j = t_j = 0.05t_u$, e) $l_j = h_j = t_j = 0.20t_u$.

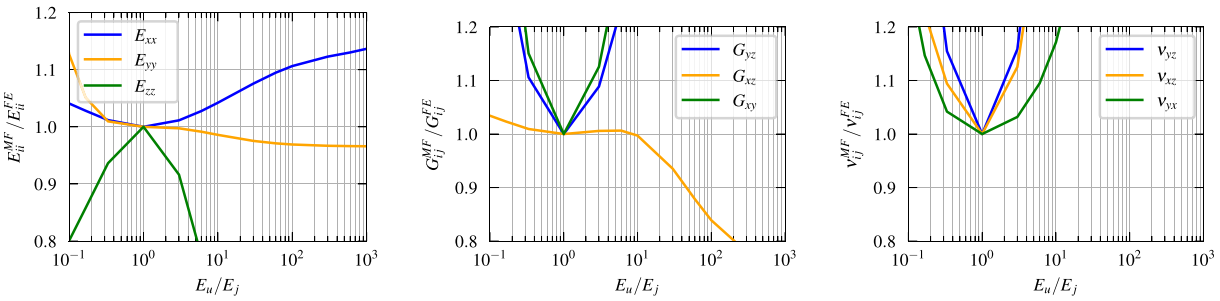

Fig. 13. Results of parametric analysis for reference values using the plain Mori-Tanaka scheme for running bond masonry.

Table 11
Comparison of proposed scheme with the model proposed by Zhou et al. in terms of mean absolute error compared with FE analyses.

Model	E_{xx}	E_{yy}	E_{zz}	G_{xy}	G_{xz}	G_{yz}	ν_{xy}	ν_{xz}	ν_{yz}
Zhou et al.	8.8%	5.3%	31.0%	4.2%	6.0%	2.8%	7.6%	3.0%	5.7%
Proposed model	1.2%	1.1%	18.2%	2.0%	2.3%	1.0%	15.9%	19.3%	17.8%

composed of units stiffer than the mortar, corresponding to traditional and historic masonry typologies. Despite the width of the parametric investigation, the accuracy of the scheme in predicting the properties of thin-joint and block masonry with perforated or otherwise orthotropic blocks has not been yet established, although the latter case is in principle within the scope of the proposed model.

The present investigation is a first step in a future line of investigation containing its implementation for nonlinear analysis of masonry shear walls. Additionally, the scheme can be implemented in a multi-scale model for three-leaf walls, accounting for the behaviour of the external leaves of the structure.

Improvements of the model to be pursued in future include a move from the semi-empirical determination of the participation factors to a more robust calculation according to geometric and relative stiffness parameters of the material phases. Additionally, an improvement in the prediction of the transversal stiffness of double-wythe typologies, namely, English and Flemish bond, for highly deformable mortar is also motivated.

Declaration of Competing Interest

The authors declare that they have no known competing financial interests or personal relationships that could have appeared to influence the work reported in this paper.

References

[1] Aboudi J, Pindera M-J. Micromechanics of Metal Matrix Composites Using the Generalized Method of Cells Model (GMC) - User's Guide. NASA; 1992.

[2] Addessi D, Di Re P, Sacco E. Micromechanical and multiscale computational modeling for stability analysis of masonry elements. Engineering Structures 2020; 211:110428.

[3] Alnæs, Martin S., Jan Blechta, Johan Hake, August Johansson, Benjamin Kehlet, Anders Logg, Chris Richardson, Johannes Ring, Marie E. Rognes, and Garth N. Wells. 2015. 'The FEniCS Project Version 1.5'. *Archive of Numerical Software* 3 (100). 10.11588/ans.2015.100.20553.

[4] Bati SB, Ranocchiai G, Ranocchiai G, Rovero L. A Micromechanical Model for Linear Homogenization of Brick Masonry. Materials and Structures 1999;32(1): 22–30.

[5] Cavalagli N, Cluni F, Gusella V. Evaluation of a Statistically Equivalent Periodic Unit Cell for a Quasi-Periodic Masonry. International Journal of Solids and Structures 2013;50(25–26):4226–40. https://doi.org/10.1016/j.ijsolstr.2013.08.027.

[6] Cavalagli N, Cluni F, Gusella V. Failure Surface of Quasi-Periodic Masonry by Means of Statistically Equivalent Periodic Unit Cell Approach. Meccanica 2018;53 (7):1719–36. https://doi.org/10.1007/s11012-017-0771-5.

[7] Cecchi A, Sab K. A homogenized Reissner–Mindlin model for orthotropic periodic plates: Application to brickwork panels. International Journal of Solids and Structures 2007;44(18-19):6055–79.

[8] Drougkas A. Macro-Modelling of Orthotropic Damage in Masonry: Combining Micro-Mechanics and Continuum FE Analysis. Engineering Failure Analysis 2022; 141:106704. https://doi.org/10.1016/j.engfailanal.2022.106704.

[9] Drougkas A, Licciardello L, Rots JG, Esposito R. In-Plane Seismic Behaviour of Retrofitted Masonry Walls Subjected to Subsidence-Induced Damage. Engineering Structures 2020;223:111192. https://doi.org/10.1016/j.engstruct.2020.111192.

[10] Drougkas A, Roca P, Molins C. Experimental Analysis and Detailed Micro-Modeling of Masonry Walls Subjected to In-Plane Shear. Engineering Failure Analysis 2019; 95:82–95. https://doi.org/10.1016/j.engfailanal.2018.08.030.

[11] Drougkas A, Sarhosis V. Micro-Mechanical Homogenisation of Three-Leaf Masonry Walls under Compression. Engineering Structures 2021;245:112890. https://doi.org/10.1016/j.engstruct.2021.112890.

[12] Drougkas A, Sarhosis V, D'Alessandro A, Ubertini F. Homogenisation of Masonry Structures Subjected to Seismic Loads through Matrix/Inclusion Micromechanics. Structures 2022;38:375–84. https://doi.org/10.1016/j.istruc.2022.02.016.

[13] Drougkas A, Verstrynge E, Hayen R, Van Balen K. The Confinement of Mortar in Masonry under Compression: Experimental Data and Micro-Mechanical Analysis. International Journal of Solids and Structures 2019;162:105–20. https://doi.org/10.1016/j.ijsolstr.2018.12.006.

[14] Drougkas A, Verstrynge E, Szekér P, Heirman G, Bejarano-Urrego L-E, Giardina G, et al. Numerical Modeling of a Church Nave Wall Subjected to Differential Settlements: Soil-Structure Interaction, Time-Dependence and Sensitivity Analysis. International Journal of Architectural Heritage 2020;14(8):1221–38. https://doi.org/10.1080/15583058.2019.1602682.

[15] Eshelby, J. D. 1957. 'The Determination of the Elastic Field of an Ellipsoidal Inclusion, and Related Problems'. *Proceedings of the Royal Society of London. Series A, Mathematical and Physical Sciences* 241(1226):376–96.

[16] Foulger GR, Wilson MP, Gluyas JG, Julian BR, Davies RJ. Global Review of Human-Induced Earthquakes. Earth-Science Reviews 2018;178:438–514.

[17] García-Macías E, Ubertini F. Earthquake-induced damage detection and localization in masonry structures using smart bricks and Kriging strain reconstruction: A numerical study: Earthquake-induced damage detection using smart-bricks. Earthquake Engng Struct Dyn 2019;48(5):548–69.

[18] Geers, Marc G. D., Varvara G. Kouznetsova, Karel Matouš, and Julien Yvonnet. 2017. 'Homogenization Methods and Multiscale Modeling: Nonlinear Problems'. Pp. 1–34 in *Encyclopedia of Computational Mechanics Second Edition*. American Cancer Society.

[19] Grzyb K, Jasiński R. Parameter estimation of a homogeneous macromodel of masonry wall made of autoclaved aerated concrete based on standard tests. Structures 2022;38:385–401.

[20] Hill R. The Essential Structure of Constitutive Laws for Metal Composites and Polycrystals. Journal of the Mechanics and Physics of Solids 1967;15(2):79–95.

[21] Lagomarsino S, Cattari S. PERPETUATE Guidelines for Seismic Performance-Based Assessment of Cultural Heritage Masonry Structures. Bulletin of Earthquake Engineering 2015;13(1):13–47. https://doi.org/10.1007/s10518-014-9674-1.

[22] Lielens G. Micro-Macro Modeling of Structured Materials. Université catholique de Louvain, Louvain-la-Neuve; 1999. PhD dissertation,.

[23] Lourenço PB, Pina-Henriques JL. Validation of Analytical and Continuum Numerical Methods for Estimating the Compressive Strength of Masonry. Computers and Structures 2006;84(29–30):1977–89. https://doi.org/10.1016/j.compstruc.2006.08.009.

[24] Luo Y. Improved Voigt and Reuss Formulas with the Poisson Effect. Materials 2022; 15(16):5656. https://doi.org/10.3390/ma15165656.

[25] Massart TJ, Peerlings RHJ, Geers MGD. Structural Damage Analysis of Masonry Walls Using Computational Homogenization. International Journal of Damage Mechanics 2007;16(2):199–226. https://doi.org/10.1177/1056789506064943.

[26] Massart TJ, Peerlings RHJ, Geers MGD. Mesoscopic Modeling of Failure and Damage-Induced Anisotropy in Brick Masonry. European Journal of Mechanics A/Solids 2004;23(5):719–35. https://doi.org/10.1016/j.euromechsol.2004.05.003.

[27] Mori, T., and K. Tanaka. 1973. 'Average Stress in Matrix and Average Elastic Energy of Materials with Misfitting Inclusions'. *Acta Metallurgica* 21(5):571–74. 10.1016/0001-6160(73)90064-3.
[28] Mura T. Micromechanics of Defects in Solids: Mechanics of Elastic and Inelastic Solids. Netherlands: Springer; 1987.
[29] Pelà L, Cervera M, Roca P. Continuum Damage Model for Orthotropic Materials: Application to Masonry. Computer Methods in Applied Mechanics and Engineering 2011;200(9–12):917–30. https://doi.org/10.1016/j.cma.2010.11.010.
[30] Pierard O, Friebel C, Doghri I. Mean-field homogenization of multi-phase thermo-elastic composites: a general framework and its validation. Composites Science and Technology 2004;64(10-11):1587–603.
[31] Reuss A. Berechnung der Fließgrenze von Mischkristallen auf Grund der Plastizitätsbedingung für Einkristalle . Zeitschrift für Angewandte Mathematik und Mechanik 1929;9(1):49–58.
[32] Routh EJ. 'Theorems on the Attraction of Ellipsoids for Certain Laws of Force Other than the Inverse Square'. *Philosophical Transactions of the Royal Society of London.* Series A 1895;186:897–950.
[33] Taliercio, Alberto. 2018. 'Closed-Form Expressions for the Macroscopic Elastic Constants of Flemish Bond Masonry Walls'. Pp. 1721–31 in *10th International Masonry Conference, Milan*.
[34] Theodossopoulos D, Sinha BP. A Review of Analytical Methods in the Current Design Processes and Assessment of Performance of Masonry Structures. Construction and Building Materials 2013;41:990–1001. https://doi.org/10.1016/j.conbuildmat.2012.07.095.
[35] Voigt W. Ueber die Beziehung zwischen den beiden Elasticitätsconstanten isotroper Körper. Ann. Phys. 1889;274(12):573–87.
[36] Wilding BV, Godio M, Beyer K. The Ratio of Shear to Elastic Modulus of In-Plane Loaded Masonry. Materials and Structures 2020;53(2):40. https://doi.org/10.1617/s11527-020-01464-1.
[37] Zheng, Q. S., and D. X. Du. 2001. 'An Explicit and Universally Applicable Estimate for the Effective Properties of Multiphase Composites Which Accounts for Inclusion Distribution'. *Journal of the Mechanics and Physics of Solids* 49(11):2765–88. /10.1016/S0022-5096(01)00078-3.
[38] Zhou Y, Sluys LJ, Esposito R. An Improved Mean-Field Homogenization Model for the Three-Dimensional Elastic Properties of Masonry. European Journal of Mechanics A/Solids 2022;96:104721. https://doi.org/10.1016/j.euromechsol.2022.104721.
[39] Zucchini A, Lourenço PB. A Micro-Mechanical Model for the Homogenisation of Masonry. International Journal of Solids and Structures 2002;39(12):3233–55. https://doi.org/10.1016/S0020-7683(02)00230-5.